

Article

Occurrence Relationship between Sodium and Maceral Groups in Subbituminous Coal: A Case Study on Zhundong Coal and Shenhua Coal

Xin He ¹ , Wenfeng Wang ^{2,3,*}, Yitao Yang ², Changchun Zhou ¹ , Jingfeng He ¹, Piaopiao Duan ² and Qingfeng Lu ² 

¹ Key Laboratory of Coal Processing & Efficient Utilization, Ministry of Education, School of Chemical Engineering and Technology, China University of Mining & Technology, Xuzhou 221116, China

² School of Resources and Geosciences, China University of Mining & Technology, Xuzhou 221116, China

³ School of Geology and Mining Engineering, Xinjiang University, Urumqi 830047, China

* Correspondence: wangwenfeng@cumt.edu.cn; Tel.: +86-137-7588-1179

Abstract: The occurrence characteristics of sodium and its potential relationship with macerals in Zhundong coal, as well as in Shenhua coal with average sodium levels, are investigated in this study. A new five-step sequential extraction method was first conducted for determination. The occurrence status of sodium and its related macerals in samples was determined by microscope and SEM-EDS (scanning electron microscope-energy dispersive X-ray spectroscopy). Soluble sodium salts (H_2O-Na) make up the primary proportion of sodium in Zhundong coal, at approximately 50%, while various sodium species are distributed in Shenhua coal with nonobvious differences. Inertinite contains more sodium than vitrinite does in both coals, and the highest enrichment degree of sodium was discovered in inertinite from Zhundong coal, which presented primarily as NaCl crystals (H_2O-Na) in fusinite cells, with a local weight percentage of over 15%. More specifically, H_2O-Na and insoluble Na both tend to enrich in fusinite. Additionally, it is found that maceral-rich products can be gathered using triboelectrostatic separation, and a portion of sodium can thus be removed from the coal by removing inertinite. This study may provide new insights and references regarding sodium removal from Zhundong coal.



Citation: He, X.; Wang, W.; Yang, Y.; Zhou, C.; He, J.; Duan, P.; Lu, Q. Occurrence Relationship between Sodium and Maceral Groups in Subbituminous Coal: A Case Study on Zhundong Coal and Shenhua Coal. *Minerals* **2023**, *13*, 122. <https://doi.org/10.3390/min13010122>

Academic Editor: Saeed Chehreh Chelgani

Received: 29 October 2022

Revised: 16 December 2022

Accepted: 11 January 2023

Published: 13 January 2023



Copyright: © 2023 by the authors. Licensee MDPI, Basel, Switzerland. This article is an open access article distributed under the terms and conditions of the Creative Commons Attribution (CC BY) license (<https://creativecommons.org/licenses/by/4.0/>).

1. Introduction

The recently discovered Zhundong coalfield located in Xinjiang Province sits on 39 Gt of reserves [1,2], making it an essential support for future coal consumption in China. Subbituminous coal was found to be the main rank of this coalfield, highlighted by low ash and sulfur content, high volatile matter and reactivity, and low ignition temperature [3–5]. Zhundong coal has proved highly applicable in processing methods such as combustion, pyrolysis, gasification, liquefaction, etc. In addition, Zhundong coal is also known as a typical high-alkali coal that readily causes serious fouling and slagging issues in combustors and gasification boilers [6–8]. Many current studies focus on the occurrence modes, release behaviors, and ash-deposition mechanisms of sodium, the typical alkali metal in Zhundong coal, during combustion or gasification. Water-soluble sodium is considered to be the leading occurrence mode of sodium in Zhundong coal [9,10], which would volatilize and form NaCl or Na_2SO_4 clusters in fly ash [11]. These sodium-containing clusters would be captured by the SiO_2 and Al_2O_3 in the bottom ash [12], resulting in ash-causing problems [13]. The formation characteristics of fine particles [14,15] and the role that sodium plays [16] in them during the combustion of Zhundong coal have been extensively investigated in previous reports. Moreover, studies have noted that masses of sodium tend to linger in the solid product and noticeably affect the subsequent pyrolysis and gasification

efficiency during staged liquefaction of Zhundong coal [17]. The occurrence modes of sodium play a crucial role in the volatilization and catalytic characteristics of coal in the above processes [18,19].

Nevertheless, the authors herein have found little published research regarding the potential occurrence relationship between sodium and the organic matrix, i.e., maceral groups, in Zhundong coal. Researchers [20] pointed out that the water-soluble sodium content of the inertinite-rich fraction was only slightly lower than that in raw coal after conducting flotation experiments on Zhundong coal. This potential correlation has significant implications for the chemical conversion utilization of Zhundong coal, given the stark differences in conversion activity between the macerated groups. Vitrinite, for example, plays an active oil-producing role in liquefaction, while inertinite is known as the inert component. The establishment of a relationship between sodium and macerals may facilitate sodium removal by way of maceral separation in raw coal, which would not only enhance the utilization of different qualities and conversion efficiencies of Zhundong coal, but would also help to avoid the underlying hazards caused by sodium. However, the specific occurrence relationships between sodium and maceral groups in Zhundong coal and their separation effects have not been paid serious attention.

In this study, Zhundong coal with a prominent sodium level, sampled from the Yihua Coal Mine in Xinjiang province, was employed for sodium-occurrence investigation. A subbituminous coal with an average sodium level, sampled from the Daliuta Coal Mine in the Shenfu coalfield, Shaanxi province, was also adopted for comparison. The main objectives of the research herein are to (a) determine the contents of different occurrence modes of sodium in both raw coals and their extracted maceral samples by adopting a new five-step sequential extraction; (b) observe the specific occurrence status of sodium in collected samples and reveal its potential relationship with macerals by combined measurement of microscopy and SEM—EDS; and (c) evaluate the maceral separation and sodium removal effects of triboelectrostatic separation on both subbituminous coals.

2. Geological Setting

The Yihua Coal Mine (Figure 1, sampling location 1) of the Zhundong coalfield, Junggar Basin, is located in Jimusaer County, Changji Hui Autonomous Prefecture, Xinjiang Province, northwest China [21–23]. The main workable coal seams of the basin reside in the Middle Jurassic Xishanyao Formation (J_2x), which can be subdivided into the Upper and Lower Members [24]. The Lower Member of the Xishanyao Formation consists primarily of sandstone, siltstone, silty mudstone, mudstone, and the main workable coal seams (average thickness of ~68 m). The formation in this research area only contains one thick coal seam that is deposited in a shallow lake environment [25].

The Daliuta Coal Mine (Figure 1, sampling location 2) in the Shenfu coalfield, north-eastern Ordos Basin, is located in Shenmu County, Shaanxi Province. The second-largest inland sedimentary basin in China [26], the Ordos Basin is situated west of the Northern China Platform [27] and is famous for abundant coal deposits [28]. There are three sets of coal formation sequences in the Ordos Basin [29]: Carboniferous–Permian, Triassic, and Jurassic. The Lower Middle Jurassic Yan'an Formation (J_2y) is the main coal-bearing stratum in not only the sampling area but also the whole basin [30]. With a total thickness of 180~200 m, this formation is made up of sandstone, mudstone, and coal, which generally contains five coal seams (seams II–VI) with the thickest exploitable seam being 7~8 m [31].

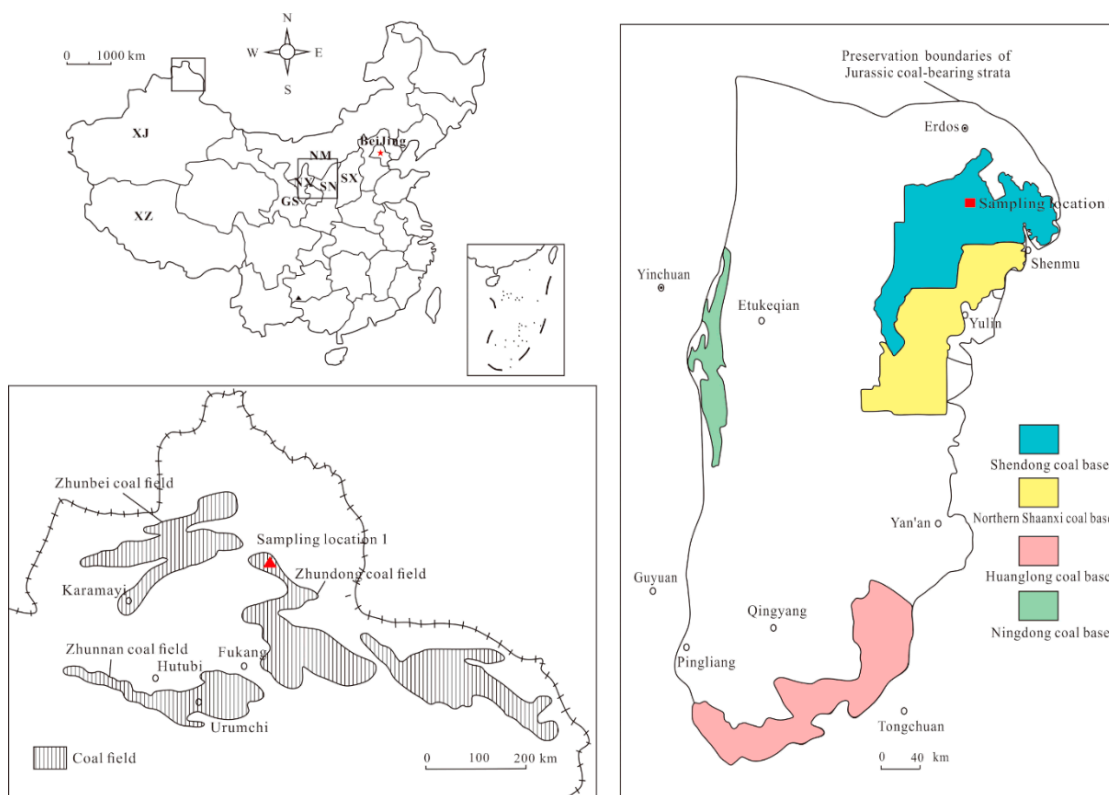


Figure 1. Locations of the Yihua and Daliuta Mines in China.

3. Materials and Methods

3.1. Sample Preparation

In this investigation, two raw coals (YHR and DLTR) were collected from the Yihua Coal Mine and Daliuta Coal Mine, respectively. Vitrinite and inertinite fractions with high purity were also extracted from the two raw coals. The liptinite group was excluded in this study owing to its extremely low content (<3%) in both raw coals [32–34]. The extraction was a fully manual operation with no chemical contact, with the aim of maximizing the preservation of the authentic status of maceral groups. A brief description of maceral extraction is as follows: Vitrain, the macrolithotype of which is abundant with vitrinite, was selected from raw coal bulks of moderate size by using a small hammer and slice blades; this step resulted in the preliminary concentration of the vitrinite group. Similarly, the preliminary concentration of the inertinite group was obtained by collecting fusain grains. Then, the vitrain and fusain collections were crushed into particles (~3 mm) for sorting. Next, the vitrain and fusain particles were scrutinized, and impurities with nonuniform texture were removed with pointed tweezers. The final vitrinite and inertinite samples obtained in this way were labeled as YHV, YHI, DLTV, and DLTI, referring to vitrinite collected from YHR, inertinite from YHR, vitrinite from DLTR, and inertinite from DLTR, respectively. Detailed operation procedures are described in previous work [35] by our group and will not be repeated here. A total of 6 samples (2 raw coals, 4 extracted maceral samples) were employed in this study.

3.2. Sample Characterization

Proximate analyses (determination of moisture content, ash yield, and volatile matter) and a total sulfur test of six samples (two raw coals and four maceral enrichments) were conducted according to China national standards GB/T212-2008 and GB/T214-2007, respectively. Ultimate analyses, including carbon, hydrogen, oxygen, and nitrogen contents, were performed based on GB/T19227-2008 and GB/T476-2008. The main compositions of YHR and DLTR, including SiO₂, Al₂O₃, Fe₂O₃, Na₂O, K₂O, MgO, CaO, S, and Cl, were

measured by an X-ray fluorescence spectrometer (S8 Tiger, Bruker, Germany). All above tests were repeated twice for accuracy of measurement.

Prior to the microscopic examination, all samples underwent crushing, screening, embedding in epoxy resin, cutting, and polishing procedures. Based on the ICCP System 1994 [36–39], maceral identification and the vitrinite random reflectance test were performed on treated samples by an optical microscope (Imager M1 m, Carl Zeiss, Jena, Germany) in conjunction with a microphotometer (MPV-SP, CRAIC, San Dimas, CA, USA). A scanning electron microscope (SIGMA, Carl Zeiss, Jena, Germany) coupled with energy-dispersive X-ray spectroscopy (EDS) was employed for surface microtopography observation and semiquantitative elemental analyses of the above samples.

3.3. Sequential Extraction Procedure

The sequential extraction procedure is the most accurate protocol for determining the occurrence mode of sodium content in coal. In general, a four-step procedure is the most commonly used operation [40–42], which adopts deionized water, ammonium acetate (NH_4OAc), hydrochloric acid (HCl), and acids for digestion (e.g., HNO_3 and HF) as four sequential solutions. Based on the above steps, Na is classified into four types: “ $\text{H}_2\text{O-Na}$ ”, “ $\text{NH}_4\text{OAc-Na}$ ”, “ HCl-Na ”, and “insoluble Na”. These refer to soluble inorganic sodium salt [8,43]; sodium associated with organic matter occurring as exchangeable cations attached to carboxylic acids (carboxylate salts), phenols, chelates and other organometallic complexes [44,45]; sodium-containing acid-soluble minerals; and acid-insoluble residues, accordingly [2].

Nevertheless, there are three uncertainties about the above extraction, which are as follows: (1) The solution/coal ratio (SCR) in deionized water leaching varies across different reports, as do the agitation duration, extraction times, etc. (2) Several investigations [46,47] have pointed out that the neutral NH_4OAc solution used in the conventional method would dissolve a portion of carbonate minerals, which should be extracted by HCl solution, especially calcium and magnesium carbonates. (3) Some organically occurring sodium associations might be extracted by acids if they are not pre-removed [48,49]. The former two questions were explored in detail by [2], who noted that 100 mL/g is the appropriate SCR for sodium extraction, and that the extraction effect of a 24 h continuous agitation in deionized water is roughly equal to four runs of 1 h agitation. Concerning the second problem, they developed an approach using 0.1 mol/L NH_4Cl ($\text{pH} = 8.5$) instead of 1 mol/L NH_4OAc , to avoid overdetermination of exchangeable Ca and Mg in high-carbonate-containing coals (Zhundong coals in their case). In terms of the third issue, Grigore and Sakurovs [44] suggested inserting a step of ethylenediamine tetraacetate diamine ($\text{NH}_4\text{-EDTA}$) extraction between the NH_4OAc and HCl steps to extract sodium that is held in chelate complexes or associated with functional groups other than carboxylic groups. In addition, the effect of $\text{NH}_4\text{-EDTA}$ on crystalline mineral matter was minimized by increasing the pH of the solution with an NH_4OH buffer.

Based on the above statements, a five-step sequential extraction method is first presented (schematic of the procedure shown in Figure 2) and conducted in this study as follows:

Step 1 ($\text{H}_2\text{O-Na}$): First, 0.8 g (error 0.0002 g) of sample from the $74 \mu\text{m} \times 150 \mu\text{m}$ fraction was weighed after crushing and screening, and the sample was transferred into a precleaned and dried 100 mL centrifuge tube. Then, the tube was placed in an oscillating agitator for constant agitation (duration: 24 h, temperature: 60°C , 150 rpm). Next, the suspension was collected after centrifugation at 4000 rpm for 20 min, after which the residue was washed three times, using 10 mL of deionized water each time. Subsequently, the centrifugation operation was performed after each washing, and all the suspensions were collected into a 200 mL polypropylene bottle. Finally, the residuals were retained for the next step.

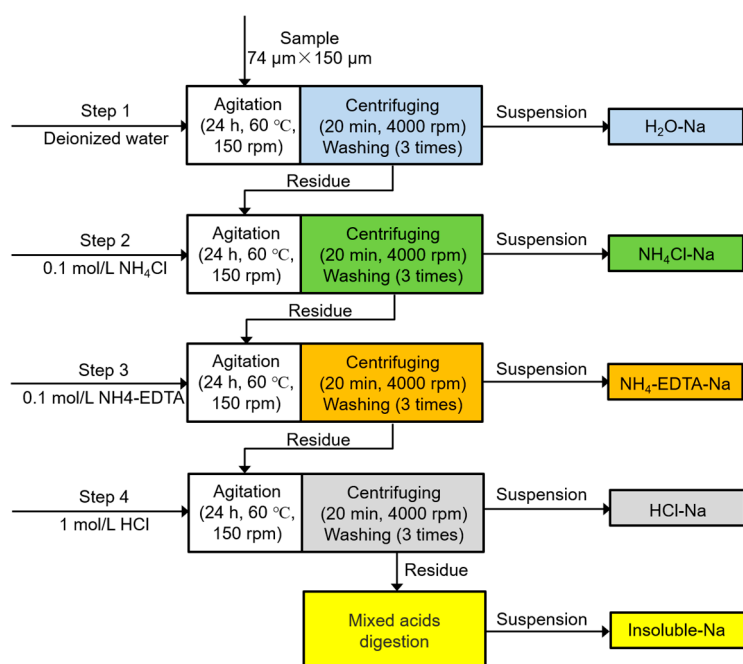


Figure 2. Diagram of sequential chemical extraction procedure.

Step 2 (NH₄Cl-Na): First, 30 mL of 0.1 mol/L NH₄Cl solution (buffered to pH 8.5 with NH₃·H₂O) was added into the centrifuge tube, which contained the residue leftover from Step 1. Then, the agitation and residue washing procedures from Step 1 were repeated with the same parameter settings. All suspensions from each centrifugation were collected for later determination, and the residue was kept for the next step.

Step 3 (NH₄-EDTA-Na): First, 30 mL of 0.1 mol/L NH₄-EDTA solution (buffered to pH 9 with NH₃·H₂O) was mixed with the residue from Step 2. Then, the rest of the operations from the previous step were repeated, including agitation, centrifugation, suspension gathering, residue washing, and preservation, as in Step 2.

Step 4 (HCl-Na): In this step, the same procedure as in Steps 2 and 3 was repeated, except that the solution applied to the residue from Step 3 was 1 mol/L HCl.

Step 5 (insoluble Na): First, the residue from Step 4 was transferred to a polytetrafluoroethylene crucible and moistened with a small quantity of deionized water. Next, 2 mL HCl ($\rho = 1.19 \text{ g/mL}$) and 2 mL HNO₃ ($\rho = 1.42 \text{ g/mL}$) were added before closing the lid, and the crucible was kept at 110 °C for 1 h. Then, 1 mL HF ($\rho = 1.13 \text{ g/mL}$) and 1 mL HClO₄ ($\rho = 1.67 \text{ g/mL}$) were added to the crucible, and it was reheated for another 2 h at 110 °C. After that, the crucible was heated up to 130 °C and maintained there for 2 h, before then being heated to 250 °C, until the smog of HClO₄ was completely evaporated. As the crucible was cooled, another 2 mL HCl (diluted with deionized water at a volume ratio of 1:9) was added to dissolve debris in the crucible. Finally, the solution was transferred into a 10 mL colorimetric tube and diluted to a standard scale with deionized water for determination.

Based on the above five-step sequential extraction method, sodium that would normally be attributed to NH₄OAc-Na or possibly dissolved by acid can instead be further subdivided into NH₄Cl-Na and NH₄-EDTA-Na. The two sodium types represent sodium associated with carboxyl groups, and sodium occurring in chelate complexes or attached to functional groups other than carboxylic groups, respectively.

An inductively coupled plasma optical emission spectrometer (ICP-OES, ICAP 6200, Thermo Fisher, Waltham, MA, USA) was employed for sodium-content determination of the suspensions collected from Steps 1~4 and the solution dissolved from residue in Step 5. Each test was repeated three times, and the mean value was recorded with the aim of guaranteeing experimental reproducibility. For comparison, the direct digestion

procedure and sodium determination were also performed on all samples in the same digestion manner as in Step 5 for the residuals.

4. Results and Discussion

4.1. Ultimate and Proximate Analyses, Total Sulfur, and Main Compositions of Samples

The total sulfur content, as well as the ultimate and proximate analyses of the six samples are presented in Table 1. As shown, YHR is characterized by higher oxygen, moisture, and volatile matter contents than DLTR. Therefore, it can be deduced that YHR has a relatively lower metamorphic grade than DLTR, although they are both classified as subbituminous coal. Moreover, both raw coals contain less than 10% ash and low total sulfur, which can be defined as low-ash coal for intensive chemical industrial utilization. The YHR sample displays extremely low ash values (3.46%), while high hydrogen content (4.59%) is shown especially by DLTR. Observing two extracted maceral samples originating from the same raw coal, vitrinite has a higher moisture and volatile matter content, while inertinite shows a higher ash content. From the perspective of ultimate analysis, vitrinite is rich in hydrogen and oxygen, whereas inertinite has abundant carbon.

Table 1. Total sulfur, and proximate and ultimate (wt%) analyses of samples.

Samples	YHR	YHV	YHI	DLTR	DLTV	DLTI
Ultimate analysis						
O _{daf}	18.48	20.32	16.14	16.91	18.25	15.30
C _{daf}	76.60	74.28	78.96	76.35	75.83	79.57
H _{daf}	3.72	4.51	3.91	4.59	4.74	4.08
N _{daf}	0.71	0.70	0.62	0.72	0.92	0.76
S _{t,d}	0.52	0.22	0.34	0.21	0.23	0.25
Proximate analysis						
M _{ad}	13.30	12.30	10.85	7.31	7.21	6.83
A _d	3.46	2.51	3.11	6.94	3.86	4.50
V _{daf}	37.93	43.07	35.20	35.60	40.12	29.97
FC _{ad}	59.82	55.48	62.84	56.74	53.48	63.42

O, oxygen; C, carbon; H, hydrogen; N, nitrogen; S_t, total sulfur; M, moisture; A, ash yield; V, volatile matter; FC, fixed carbon; daf, dry and ash-free basis; ad, air-dry basis; d, dry basis; YHR, YHV, YHI, DLTR, DLTV, and DLTI represent the two sampled raw coals and corresponding maceral samples, which are described in Section 4.1.

The main compositions, including major element oxides and common elements of two raw coals, are characterized by XRF and listed in Table 2, as along with the average values in the common Chinese coals provided by Dai et al. [50]. Both YHR and DLTR have below-average contents in the major ash components, namely SiO₂, Al₂O₃, and Fe₂O₃, which is consistent with their low-ash properties. K₂O, Na₂O, and the other two oxides of common alkali metals/alkaline earth metal elements (CaO and MgO) in YHR are all higher than the mean. Specifically, the Na₂O and MgO contents are nearly two times the average. In the case of DLTR, the contents of Na₂O, K₂O, and MgO are clearly close to or below the Chinese averages, while the CaO content is slightly higher. In short, on the basis of the above results, the two raw coals essentially exhibit their characteristic features, especially in terms of alkalinity.

Table 2. Main composition (wt%) of raw coals (on a whole-coal air-dried basis).

Samples	Na ₂ O	K ₂ O	CaO	MgO	SiO ₂	Al ₂ O ₃	Fe ₂ O ₃	S	Cl
YHR	0.302	0.006	1.740	0.458	0.167	0.428	0.145	0.717	0.048
DLTR	0.176	0.100	2.011	0.151	2.530	1.500	1.015	0.346	0.025
China ^a	0.160	0.190	1.230	0.220	8.470	5.980	4.850	nd	nd

^a, average concentrations of elements in common Chinese coals [50]; nd, no data.

4.2. Maceral Composition and Vitrinite Random Reflectance of Samples

Table 3 summarizes the results of maceral classification and vitrinite random reflectance for the six samples. YHR and DLTR are inertinite-rich coal (total inertinite 56.50%)

and vitrinite-rich coal (total vitrinite 61.50%), respectively. They both demonstrate an extremely low liptinite content (<2%), which agrees with previous reports [32–34]. The purity of maceral enrichments (YHV, YHI, DLT, and DLTI) all reached over 80%, which implies their adequate representation in this study. Collodetrinite is the dominant vitrinite maceral in the two extracted vitrinite samples (76.50% in YHV and 57.00% in DLT). Collotelinite only occurs as a small portion in YHV (11.5%), whereas its proportion rises to 27.50% in DLT. Fusinite and semifusinite are abundant in both inertinite samples. Furthermore, YHI is dominated by fusinite (48.00%), while semifusinite is the prevailing inertinite maceral (58.00%) in DLTI. A few mineral species (8.00%) were identified in DLTR, which supported the previous proximate analysis that DLTR has higher ash content than YHR.

Table 3. Maceral composition and vitrinite reflectance of samples (vol. %; on a mineral basis).

Group	Maceral	YHR	YHV	YHI	DLTR	DLTV	DLTI
Vitrinite	Telinite	2.50	3.00	2.00	3.50	7.50	2.50
	Collotelinite	2.50	11.50	0.50	3.50	27.50	1.00
	Vitrodetrinite	1.00		2.50	3.50		
	Collodetrinite	37.00	76.50	9.00	50.50	57.00	15.00
	Corpogelinite					3.00	
	Gelinite				0.50		
Total vitrinite		43.00	91.00	14.00	61.50	95.00	18.50
Inertinite	Fusinite	25.00	0.50	48.00	3.00		18.50
	Semifusinite	16.50	1.00	26.50	14.50	2.50	58.00
	Macrinite	5.00	0.50	1.50			2.00
	Micrinite	1.00	4.50	0.50	1.00	2.00	
	Inertodetrinite	9.00	2.00	8.50	10.50		2.00
Total inertinite		56.50	8.50	85.0	29.00	4.50	80.50
Liptinite	Cutinite		0.50		0.50		
	Sporinite	0.50			1.00	0.50	0.50
	Total liptinite	0.50	0.50		1.50	0.50	0.50
Minerals	Clay				2.50		
	Carbonate				3.00		
	Sulfide			1.00	2.50		
Total minerals				1.00	8.00		
Vitrinite random reflectance		0.42	0.48	0.40	0.47	0.52	0.45

4.3. Sequential Extraction Results of Samples

Figure 3 shows the distributional characteristics of sodium in the six samples, as determined by the five-step sequential extraction and ICP-OES. It is obvious that samples (YHR, YHV, and YHI) prepared from Zhundong coal have higher total sodium contents than those (DLTR, DLT, and DLTI) from Shengfu coal (Figure 3F). The total sodium content of DLTR (2164 µg/g) is approximately two-thirds of that in YHR (3196 µg/g), which is also consistent with their XRF test data. The ratios of various occurrence modes of sodium are different in the two raw coals: H₂O-Na, with an approximately 50% proportion, is the dominant occurrence mode in the YHR, and the other four modes of sodium are all below 15%, in sequence as follows: NH₄Cl-Na = NH₄-EDTA-Na > HCl-Na > insoluble Na. The primary sodium species (29%) in the DLTR is NH₄Cl-Na, followed by H₂O-Na (25%) and insoluble Na (21%) with slightly lower proportions, followed finally by the remaining modes, which have relatively low shares of approximately 10% with no significant difference.

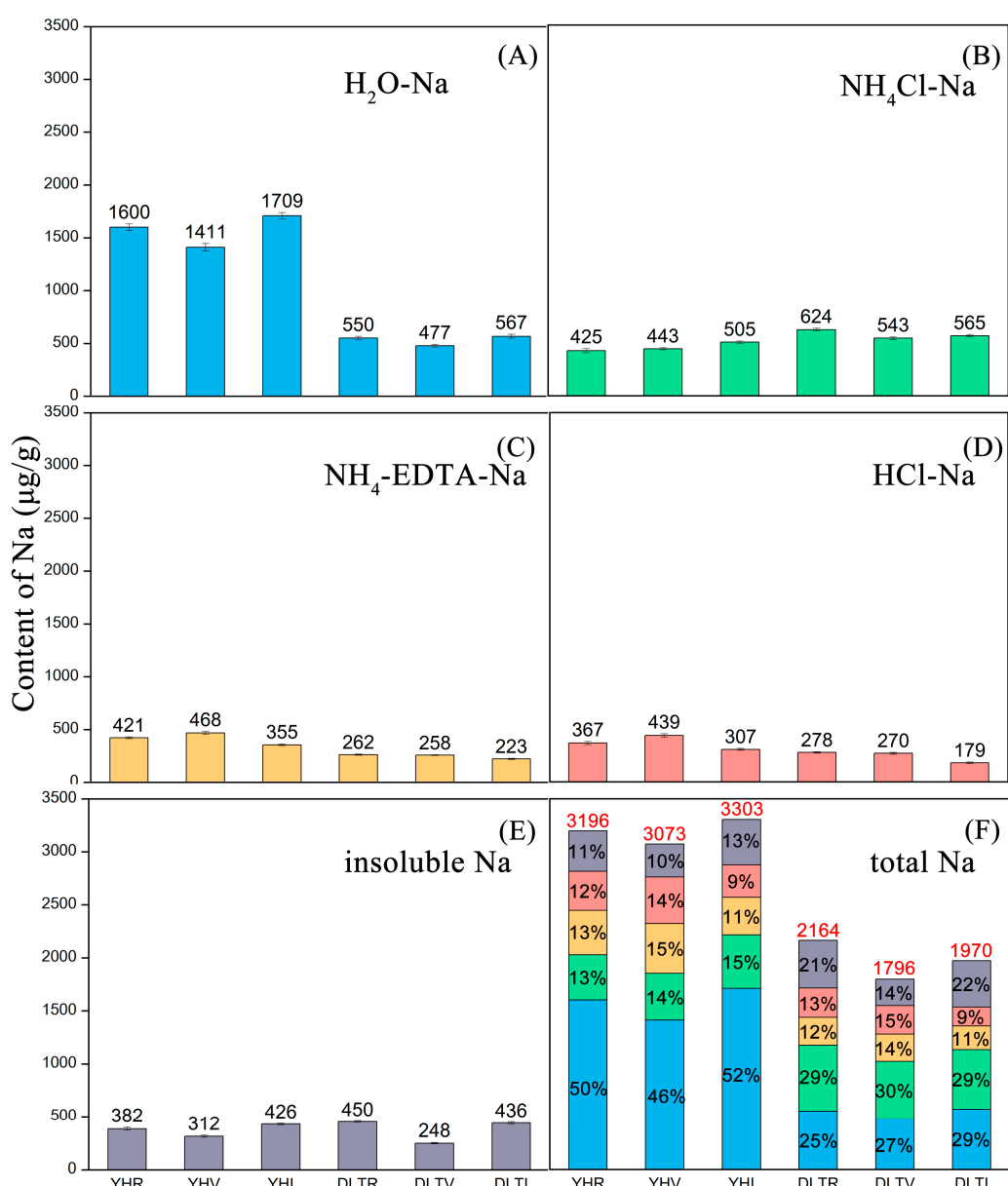


Figure 3. Content distribution characteristics of sodium in samples. (A) distribution of $\text{H}_2\text{O}\text{-Na}$; (B) distribution of $\text{NH}_4\text{Cl}\text{-Na}$; (C) distribution of $\text{NH}_4\text{-EDTA}\text{-Na}$; (D) distribution of $\text{HCl}\text{-Na}$; (E) distribution of insoluble Na; (F) distribution of total Na.

Comparing the sodium content between the two maceral groups, inertinite has a higher total sodium content than vitrinite in both coals, and this is especially pronounced in the case of Zhundong coal, indicating that sodium enriches in inertinite and that this tendency is much more prominent in Zhundong coal. A comparison between YHV and YHI shows that, despite $\text{H}_2\text{O}\text{-Na}$ accounting for the largest proportion in both samples, YHI still has a higher content and ratio of $\text{H}_2\text{O}\text{-Na}$ than YHV or YHR. YHV has a similar pattern of sodium distribution to YHR, whereas YHI exhibits a difference, with $\text{HCl}\text{-Na}$ playing the role of the least abundant mode instead of insoluble Na, demonstrating that different sodium occurrence modes show various affinities with macerals. In the case of Zhundong coal, YHV does not show a particular attraction to any kind of sodium, while $\text{H}_2\text{O}\text{-Na}$ and insoluble Na tend to concentrate in YHI. For Shengfu coal, DLTI essentially shares similar distribution patterns with raw coal, except that the $\text{H}_2\text{O}\text{-Na}$ ratio is slightly higher at 29% and the $\text{HCl}\text{-Na}$ ratio is lower at 9%. Instead of $\text{HCl}\text{-Na}$, insoluble Na has

the lowest content with a distinct drop in DLT. In conclusion, H₂O-Na and insoluble Na are easily gathered in inertinite, while HCl-Na tends to concentrate in vitrinite.

4.4. Sodium Occurrence Characteristics in Macerals

4.4.1. Sodium Occurrence Characteristics of Shenfu Coal

For the purpose of identifying the occurrence status of sodium and confirming which macerals it is associated with, all samples were first tested by SEM-EDS for the detection and position tagging of sodium-containing particles. Then, microscopic observations were performed to analyze the maceral composition of sodium-containing particles. It should be noted that, despite the fact that basic profiles and characteristics of particles can be roughly consistent under SEM and microscopy, a few delicate differences in morphology are unavoidable due to the pre-measurement grinding and polishing.

Vitrinite and inertinite particles were cross-dispersed in the DLTR sample, with some minerals occasionally filled in, and no trace of sodium was found. As shown in Figure 4, two typical particles were displayed. One is mainly composed of telinite with calcite filling in deformed cells and fractures (Figure 4A,B), while the other comprises fusinite and cell-filling kaolinite (Figure 4C,D). Vitrinite is the predominant maceral group in almost all particles in DLT, while a small amount of inertinite and minerals are characterized by scattered distribution. The two chosen particles demonstrate the common state of DLT. Collodetrinite and collotelinite make up the major proportion of coal particles, whereas the other macerals are dispersed among them (Figure 5A,C); occasionally, slight minerals such as quartz, pyrite, and kaolinite are embedded on the surface or filled in the fractures/cells (Figure 5B,D).

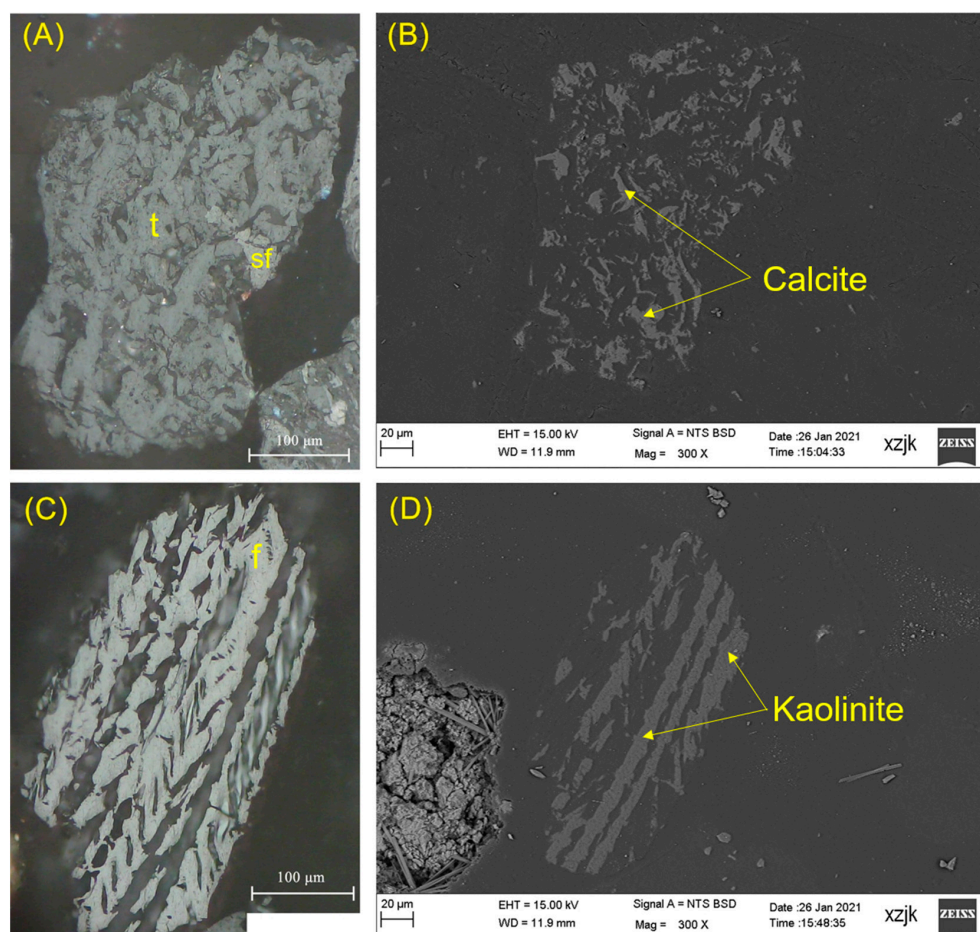


Figure 4. Microscope and SEM-EDS identification of DLTR: (A) A telinite (t) mixed with semifusinite (sf) fragment; (B) SEM-EDS image of (A); (C) A fusinite (f) particle; (D) SEM-EDS image of (C).

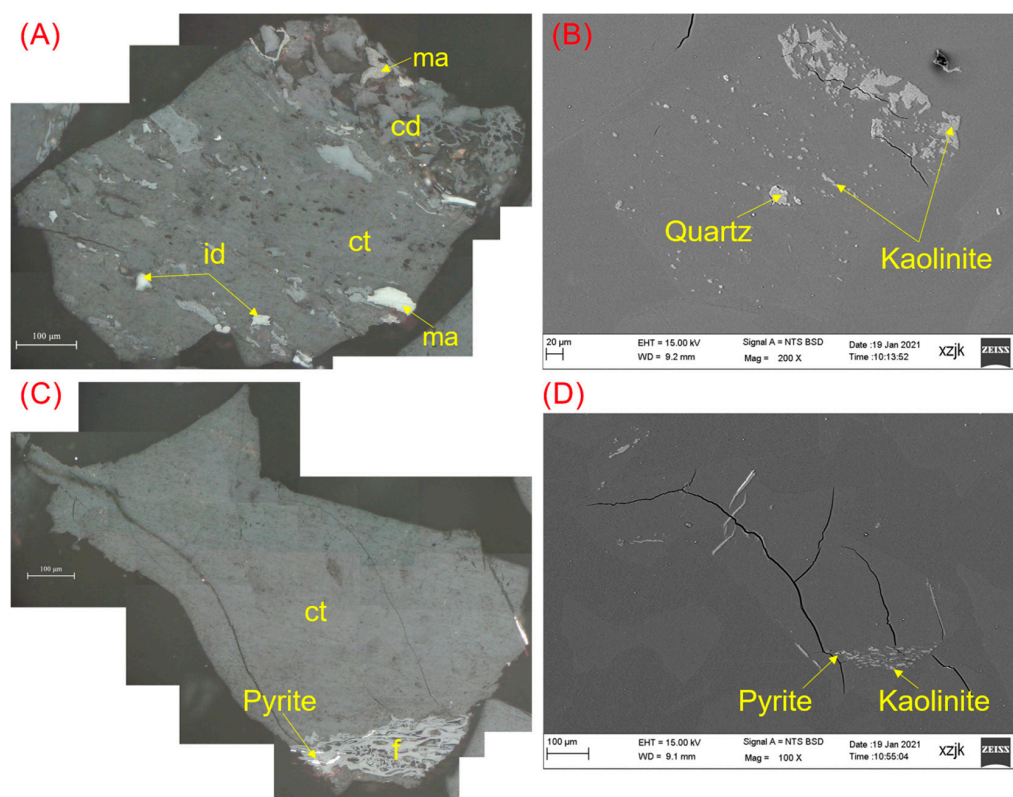


Figure 5. Microscope and SEM–EDS identification of DLT. **(A)** A particle composed of large-area collotelinite (*ct*) and some collodetrinitite (*cd*) with specked inertodetrinitite (*id*) and macrinitite (*ma*); **(B)** SEM–EDS image of **(A)**; **(C)** A collotelinite (*ct*) particle intruded by a small piece of fusinite (*f*) with cell-filling pyrite; **(D)** SEM–EDS image of **(C)**.

In contrast to DLTR and DLT, a small amount of sodium was found in DLT. As demonstrated in Figure 6, sodium was detected in the cell-filling pyrite of a coal particle, which was observed under the microscope to be fusinite accompanied by a banded collodetrinitite. An EDS mapping covering the sodium-enriched region was analyzed and is shown in Figure 6. Fe, S, Al, Si, and Na were identified in the above area, confirming the presence of a cell-filling aluminosilicate mineral (kaolinite in this case, according to the 1:1 ratio of Al and Si), which was hard to recognize under microscopic observation. Although two associated minerals occurred in the same zone, aggregation of sodium was only found in pyrite. EDS analysis was carried out on three selected spots in the pyrite, as demonstrated in Figure 6. The identification of pyrite is indicated by the significant heights of the Fe and S K α peaks in the EDS spectrum of Spot 2, and the good 1:2 atom ratio of Fe and S. The occurrence of the Na K α peak in the spectra of Spots 1 and 3 indicates that a portion of Fe $^{2+}$ has been substituted by Na $^+$, which results in the imbalance of the Fe and S atom ratio. The substitution case differs slightly in two spots. There are other substitution elements, such as Al and Mn, in Spot 1, whereas the substitution in Spot 3 is purely Na. The weight ratios of sodium in both spots were significantly higher than the mean (0.176% in Na₂O) of DLTR in the XRF measurements, suggesting evident sodium aggregation in this pyrite zone, which also agrees with the high insoluble Na content (22%) of DLT in the above tests. Although the contents of H₂O-Na (29%) and NH₄Cl-Na (29%) are both slightly higher than that of insoluble Na in DLT, these two occurrence modes of sodium are much harder to find.

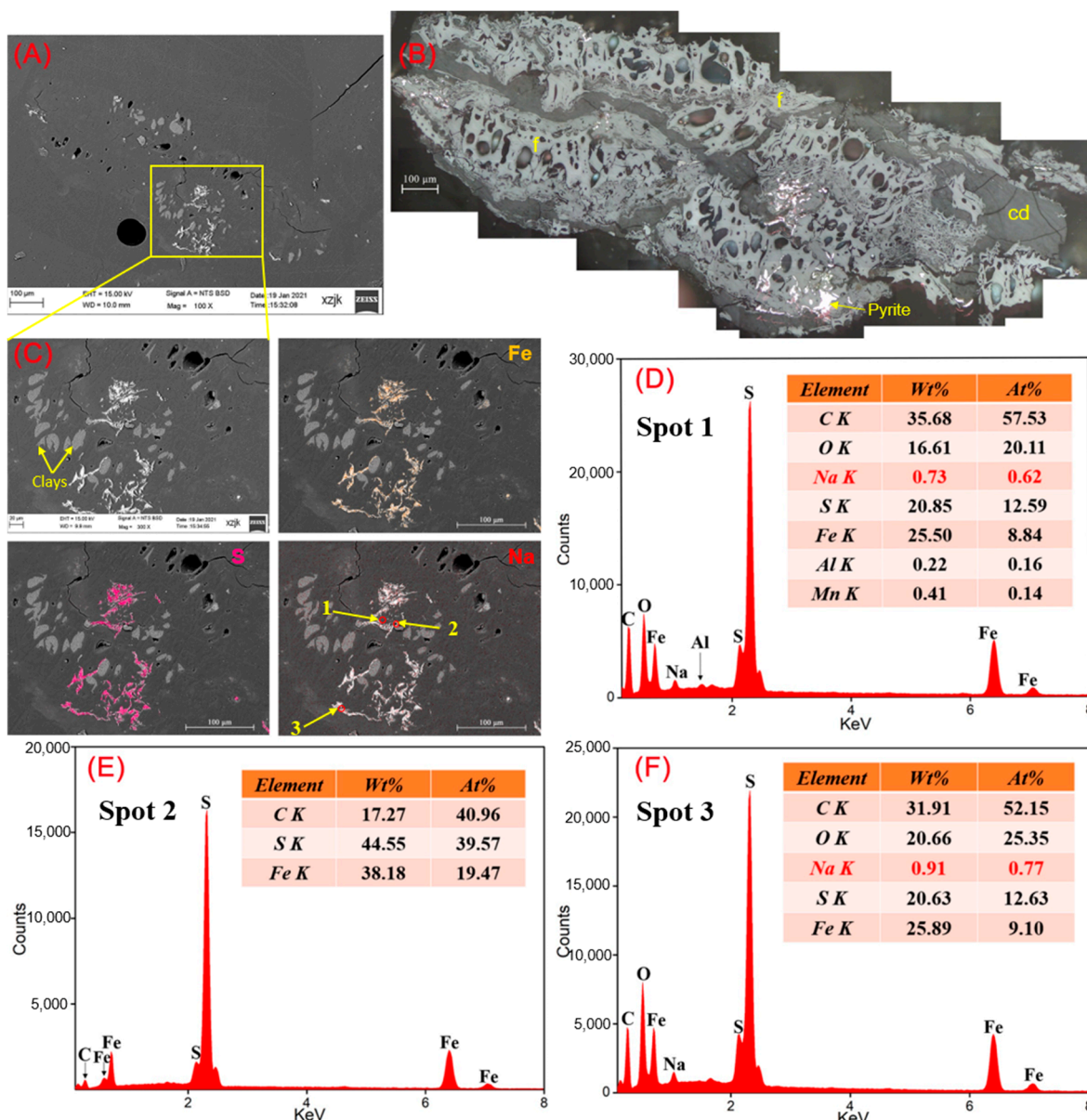


Figure 6. Microscope and SEM–EDS identification of DLTI: (A) SEM image of (B); (B) A fusinite (f) particle adorned by a long ribbon-shaped collodetrinite (cd) on edge and cracks, accompanied by some cell-filling pyrite; (C) Magnified SEM image of the yellow-boxed area in (A); (D–F) are EDS spectra from Spots 1, 2 and 3, respectively.

Considering the low ash and sodium content of samples from the DLT mine, it is necessary to discuss the possible origin and formation of the above findings. Usually, pyrite in low-sulfur coal is regarded as a direct precipitation product of divalent iron, derived from the degrading plant tissues combined with HS^- or organic sulfide [51]; such reactions occur in freshwater peat swamps. The above proposal also accords with the circumstance in the case of DLT, which comes from the middle Jurassic Yan'an Formation deposited in a confined lake environment [52]. Given the surrounding associated clay minerals, there are two possible sources of sodium in pyrite. First, as already mentioned, sodium may be mixed with sulfur in pyrite, as they are two elements that commonly co-exist in coal-forming plants. In addition, sodium may come from the associated clays as a compensation cation, along with iron, as the divalent iron in pyrite could be transformed from the trivalent iron in clays, which is reduced by organic matter in peat swamps [53].

4.4.2. Sodium Occurrence Characteristics of Zhundong Coal

Compared with DLT samples, sodium was much easier to find in all the samples from the YH mine. In YHR, Na was discovered in a coal particle sandwiched by two pieces of telinite and a semifusinite bulk (Figure 7B). Based on the SEM (Figure 7A) identification of this particle, in addition to some cell-filling kaolinite, sodium was discovered in a semifusinite cell, which was deformed and nearly disappeared under the microscope. According to the EDS spectra of two spots on the cell-filling lumps, calcite (CaCO_3) should be the main fill, and small quantities of Al, Mg, and Si were mixed as isomorphism states. In this case, a minor amount of Na along with Cl occurs as NaCl , which could be attributed to HCl-Na given its mixing with CaCO_3 . There is a slight difference between Spots 4 and 5. The content of Cl was higher than that of Na in Spot 4, while this was reversed in Spot 5, which could be interpreted as the presence of other chloride salts in Spot 4, whereas extra sodium was mixed in calcite in Spot 5.

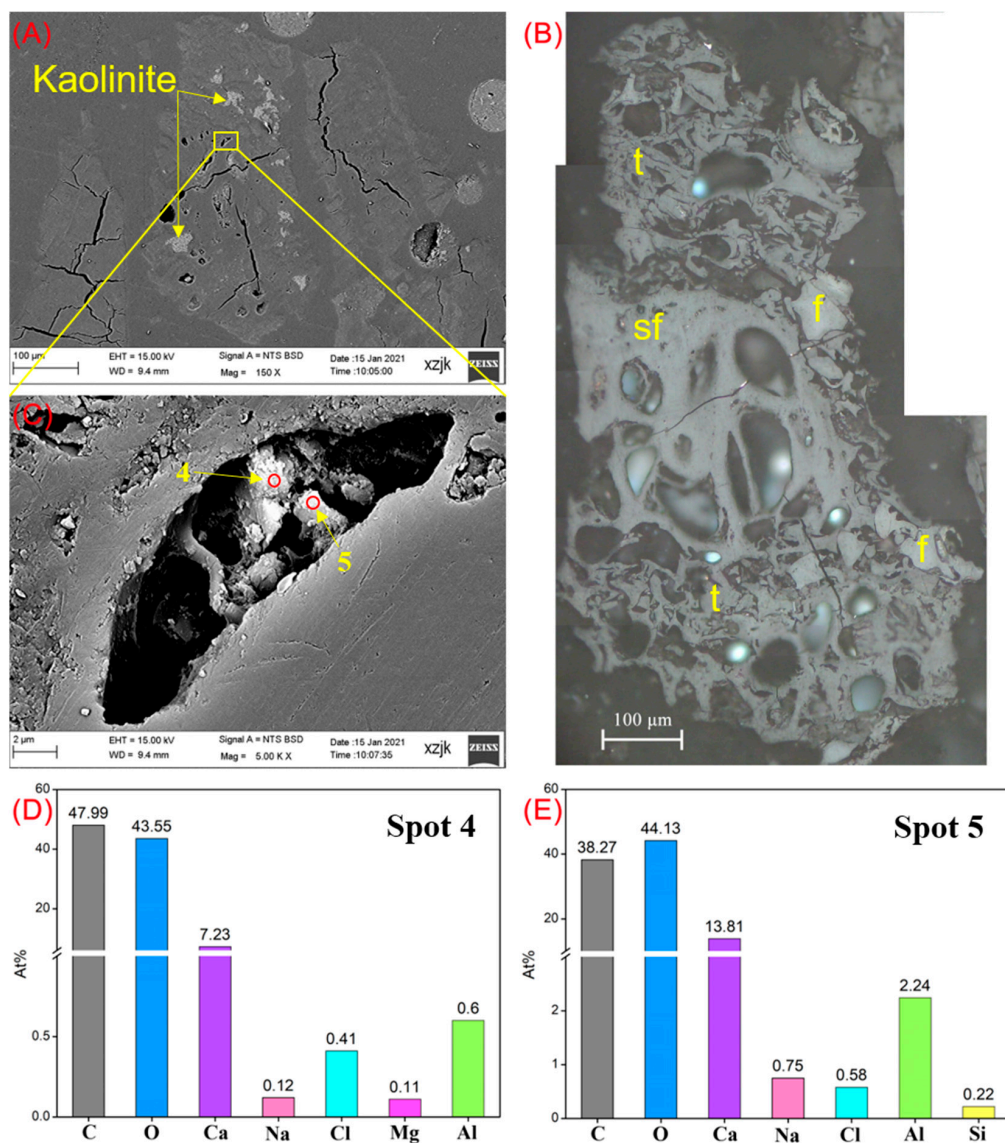


Figure 7. Microscope and SEM-EDS identification of DLTI: (A) SEM image of (B); (B) A particle sandwiched by two pieces of telinite (t) and a semifusinite (sf) bulk; (C) Magnified SEM image of the yellow-boxed area in (A); (D,E) are EDS spectra from Spots 4 and 5, respectively.

Most particles in the YHV samples were composed of colloidetrinitre, mainly due to its high vitrinite enrichment, which makes it difficult to find sodium with distinct

features, such as H₂O-Na and insoluble Na. The typical status of the particles in YHV is demonstrated in Figure 8A,B as purely collodetrinitite bulks. Their Na EDS mappings show a disordered and dispersive distribution, and the EDS spectra of randomly tested spots do not indicate any elements other than C and O.

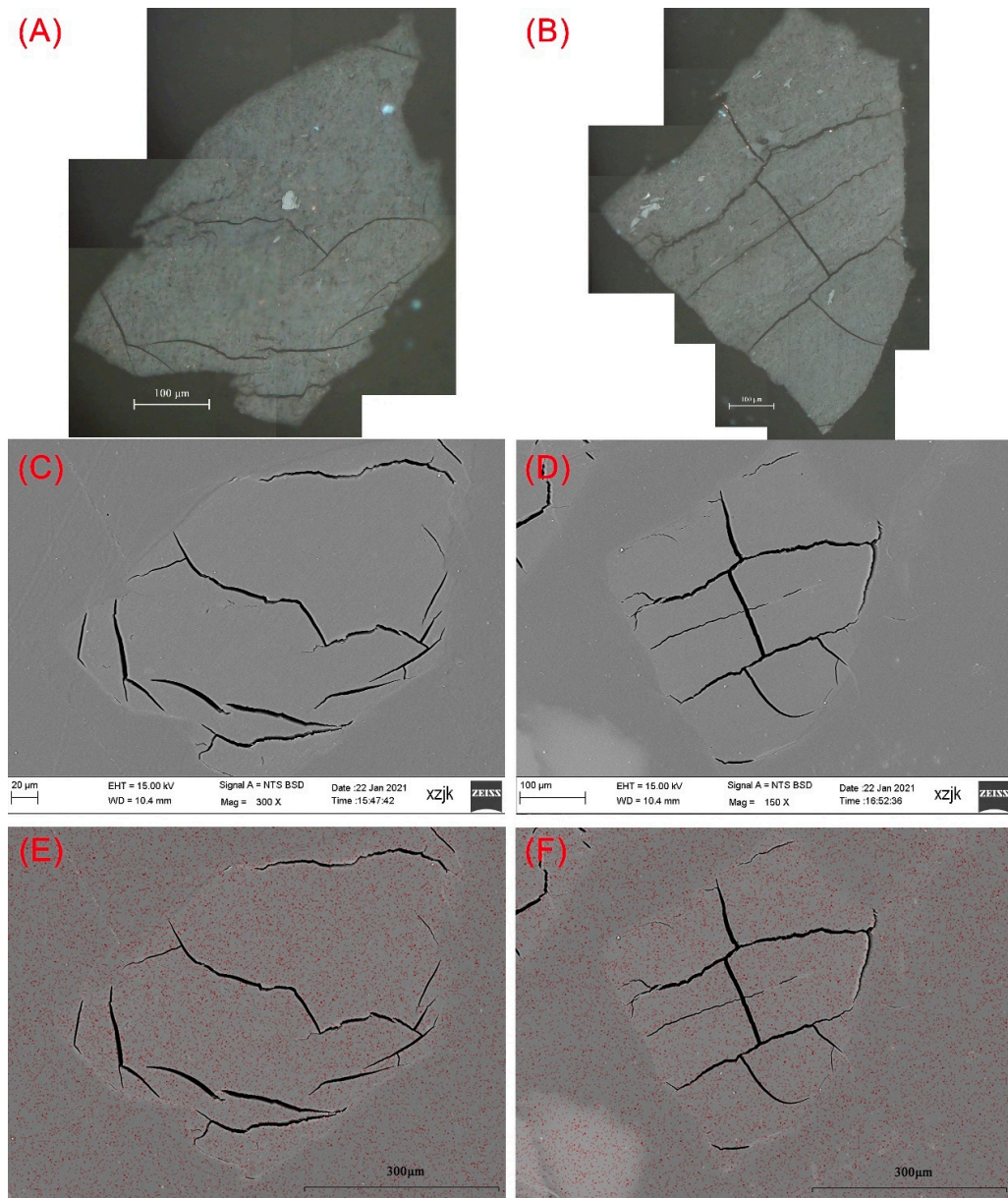


Figure 8. Microscope and SEM-EDS identification of YHV: (A,B) collodetrinitite (cd) particles; (C,D) SEM images of (A,B); (E,F) Na EDS mappings of (A,B).

As demonstrated Figure 9C, three cubic crystals in a fusinite cell of YHI could be distinctly observed and identified by EDS. The spectral data of Spots 6, 7, and 8 (Figure 9D–F) all show obvious sodium aggregation in each cube, and the enrichment extent increases with crystal size. In addition, the particular characteristics vary among them. The sodium weight percentages of Spots 6 and 7 were both over 15%, indicating a highly enriched level of Na. In view of the higher content of Cl than Na, sodium occurrence in these two crystals is basically halite (NaCl), which indicates that there are traces of other chlorides, such as KCl, MgCl₂, and CaCl₂, given the presence of these elements in the spectra. Furthermore, some Ca in Spot 7 may be attributed to calcite, considering that the Cl content is just slightly higher than that of Na in Spot 7, in addition to the usual symbiotic relationship between halite and calcite

(CaCO_3). Spot 8 is slightly different; not only does Na have a higher content than Cl, but the spot also has more S and Al, in comparison to the other two cubes, indicating a more complex occurrence case. This crystal is highly likely to be the symbiotic product of halite and calcite, and may even include some dolomite ($\text{CaMg}[\text{CO}_3]_2$). A minor amount of soluble salt, Na_2SO_4 , may exist, as well as other chlorides, such as KCl and MgCl_2 . Given the high content of Ca, this area may also contain some CaSO_4 . A small amount of Al is most likely to be present as an impurity in the mentioned substances.

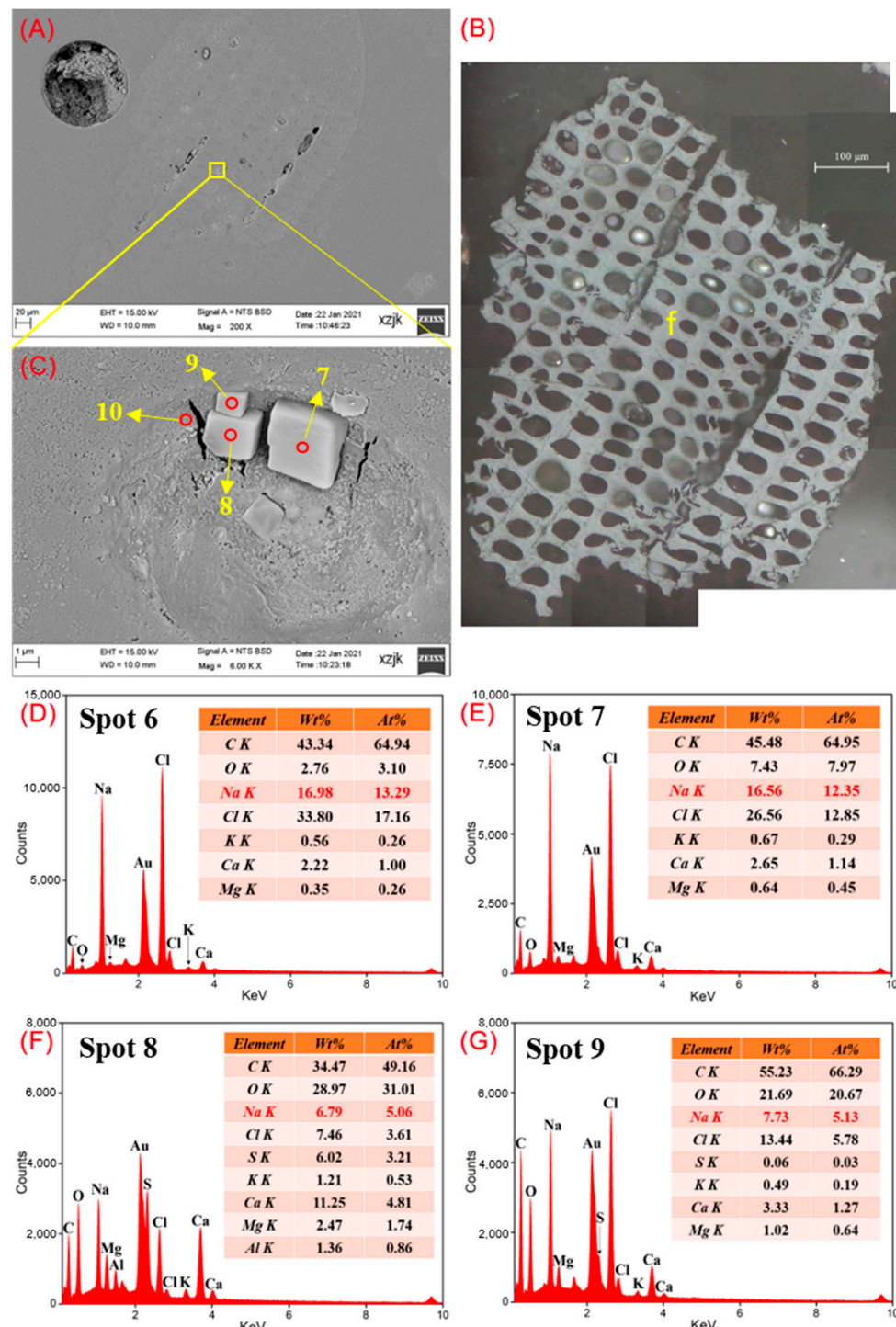


Figure 9. Microscope and SEM–EDS identification of YHI: (A) SEM image of (B); (B) A fusinite (f) particle; (C) Magnified SEM image of the cell boxed in yellow in (A); (D–G) EDS spectra from Spots 6, 7, 8, and 9, respectively.

Spot 9 was taken on the adjacent fusinite surface and tested for comprehensive analysis, which also showed sodium enrichment. NaCl was the dominant occurrence mode of Na in spot 9, and a tiny amount of Na₂SO₄ may also exist, given the presence of trace S. Considering the high content of Cl, other salts such as CaCl₂, MgCl₂, and KCl may exist, and some syngenetic CaCO₃ could also be expected due to the obvious Ca concentration. In conclusion, the Na discovered in YHI could be attributed to H₂O-Na (inorganic sodium salts), and the high aggregation level also proves its predominant role in the sodium of Zhundong coal.

4.4.3. Occurrence Relationship between Sodium and Maceral Groups

Based on the above analyses of samples from Zhundong coal and Shenfu coal by microscopy and SEM-EDS, it is obvious that inertinite samples (DLTI and YHI) have a higher frequency of detecting Na and a stronger enrichment extent of Na-containing sites than vitrinite samples (DLTV and YHV). This is also consistent with the higher total sodium content of inertinite in previous measurements. Gathering NaCl crystals (typically H₂O-Na) with a high enrichment level (over 15%) were detected in YHI. In addition, sodium associated with pyrite (insoluble Na) was uncovered in DLTI, which is quite significant considering its plain sodium content and the fact that it is more Na-rich (0.73% and 0.91% in Spots 1 and 3, respectively). Furthermore, it is worth noting that all the sodium found in inertinite is associated with fusinite, which indicates a relevancy between gathering sodium and fusinite.

Categorizing the occurrence mode of sodium in maceral groups, the evidence of inorganic sodium (H₂O-Na and insoluble Na) in inertinite is much more obvious, which also accords with the results of the above sequential extraction analysis, which found that H₂O-Na and insoluble Na are primarily focused in inertinite. Combined with the findings that fusinite appears to be a sodium-related maceral, this is mainly due to the high porosity and larger number of fractures in fusinite, which makes it easier for H₂O-Na and insoluble Na to fill in.

No sodium was identified in the vitrinite samples—not even HCl-Na, which was indicated by the extraction test to be the main sodium mode in vitrinite. Thus, the relationship between sodium and vitrinite remains unclear.

4.5. Maceral Separation on Shenfu and Zhundong Coals

Based on above analyses of occurrence relationships between sodium and maceral groups in Zhundong coal, sodium removal could be achieved by employing maceral separation of raw coal. In this study, lab-scale triboelectrostatic separation was performed on Zhundong coal; in light of its advantages in terms of both water- and cost-saving, this process is especially suitable for areas where coal is abundant but water is scarce. The schematic diagram of separation is shown in Figure 10. Raw coal first goes into the separation system through the feeding inlet. Then, under the negative pressure formed by air flow derived from the centrifugal fan, vitrinite and inertinite groups in the tribo-charging tube would receive opposite surface charges due to their different properties. Then, the charged samples are adsorbed onto two parallel high-voltage plates with opposite polarities, and are collected as clean coal and tailings products, respectively. Table 4 summarizes the yield, ash content, maceral composition, and total sodium content tested by microscopy and ICP-MS, respectively. A similar operation was also conducted on Shenfu coal to verify the general applicability of the above method of maceral separation.

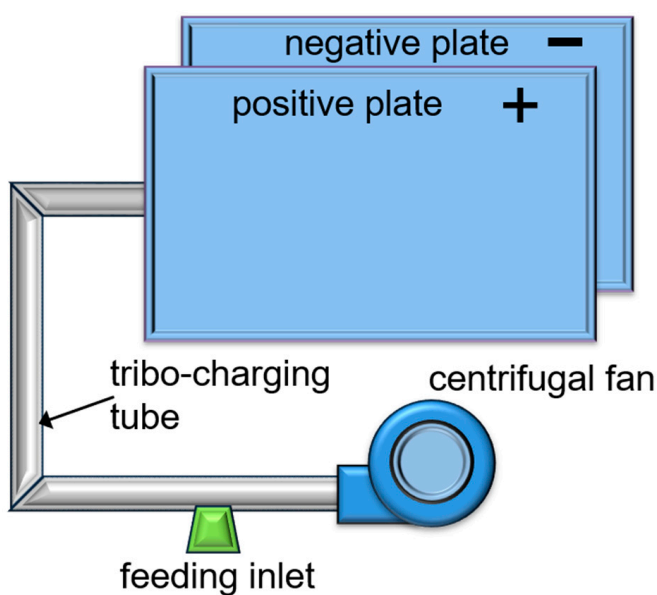


Figure 10. Schematic diagram of triboelectrostatic separation system.

Table 4. Triboelectrostatic separation results of Zhundong and Shenfu coal.

Samples	Clean Coal					Tailing				
	Yield %	AS %	VG %	IG %	TS $\mu\text{g/g}$	Yield %	AS %	VG %	IG %	TS $\mu\text{g/g}$
YHR	38.56	2.32	51.50	47.00	2679	61.44	4.18	36.50	64.00	3551
DLTR	40.37	4.13	70.50	24.50	1553	59.78	8.82	53.50	33.50	2270

AS, ash content; VG, vitrinite group content; IG, inertinite group content; TS, total sodium content.

As shown in Table 4, it is obvious that vitrinite tends to enrich in clean coal while more inertinite concentrates in the tailing after triboelectrostatic separation of both subbituminous coals. In the case of YHR, the inertinite content of tailings increased to 64.0% compared to 56.5% in raw coal, and the vitrinite content of clean coal reached 51.5% from 43.0% in raw coal. This indicates that macerals in Zhundong coal can be enriched by triboelectrostatic separation, and even better results can be obtained after parameter optimization of the separation system. Moreover, the goal of sodium removal can also be accomplished along with the maceral separation. It is clear that the total sodium content in tailings (3551 $\mu\text{g/g}$) of Zhundong coal was much higher than that in clean coal (2679 $\mu\text{g/g}$) due to the higher inertinite content of tailings. In particular, $\text{H}_2\text{O-Na}$, the main cause of fouling and slagging problems, was also separated with inertinite in tailings.

The maceral separation effect on Shenfu coal was relatively poor compared with Zhundong coal, which may be attributed to the fact that the high vitrinite content (61.5%) of DLTR already makes it close to a separation product. The inertinite content of tailings increased to 33.5% from 29% of raw coal, and the vitrinite content of clean coal went up to 70.5% from 61.5% of raw coal. Vitrinite-rich product is easily obtained from DLTR through triboelectrostatic separation. In terms of sodium removal, due to the clear bond between the inertinite and sodium, the total sodium content of tailings (2270 $\mu\text{g/g}$) was much higher than that in clean coal (1553 $\mu\text{g/g}$). The above results demonstrate that the occurrence relationship of inertinite and sodium in Zhundong coal is also valid for other subbituminous coals with an average sodium level. Furthermore, maceral separation of raw coal not only manages to remove sodium, but also provides two types of maceral-rich products for subsequent coal-staged utilization.

5. Conclusions

In this report, content determination, occurrence observation, and separation of Zhundong coal and its maceral samples were performed by sequential extraction, microscopy,

and SEM–EDS, respectively, in order to determine the occurrence relationship between sodium and maceral groups, and the feasibility of sodium removal by maceral separation. For comparison, all procedures were also conducted on a same-rank coal from Shenfu with a common sodium level. The main conclusions are drawn as follows:

- (1) In extraction, Zhundong coal has higher total sodium content than Shenfu coal. $\text{H}_2\text{O-Na}$ takes the major position in Zhundong coal with an overwhelming proportion (~50%), while the other four modes follow in descending order: $\text{NH}_4\text{Cl-Na} = \text{NH}_4\text{-EDTA-Na} > \text{HCl-Na} >$ insoluble Na. The proportion sequence of various sodium species in Shenfu coal was $\text{NH}_4\text{Cl-Na} > \text{H}_2\text{O-Na} >$ insoluble Na $> \text{HCl-Na} > \text{NH}_4\text{-EDTA-Na}$, with no obvious differences. In both cases, inertinite has higher total sodium content than vitrinite, indicating its stronger relationship with sodium. Additionally, the degree of relevancy varies with the occurrence mode of sodium, as $\text{H}_2\text{O-Na}$ and insoluble Na both tend to concentrate in inertinite, whereas vitrinite has a relatively higher HCl-Na content.
- (2) In occurrence observation, there was mildly insoluble Na gathering in the cell-filling pyrite of inertinite from Shenfu coal, whereas nothing was found in vitrinite or raw coal samples from there. In contrast, various levels of sodium enrichment were discovered in raw samples and inertinite from Zhundong coal, which presented as HCl-Na (blended with CaCO_3) and $\text{H}_2\text{O-Na}$ (NaCl crystals along with minor Na_2SO_4 , possible symbiotic minerals such as CaCO_3 and $\text{CaMg}[\text{CO}_3]_2$), respectively. In addition, no sodium was discovered in vitrinite from Zhundong coal. Thus, sodium is much more likely to aggregate in inertinite than in vitrinite; additionally, it has a stronger enrichment degree in inertinite, and the local weight percentage of sodium in NaCl crystals was over 15%. This is also consistent with the earlier extraction results; $\text{H}_2\text{O-Na}$ and insoluble Na tend to appear in inertinite, more specifically, fusinite, which should be mainly attributed to the space provided by its abundant pores and fractures. Given that no sodium was identified in vitrinite samples, the relationship between them could not be generalized in this case.
- (3) A certain degree of maceral enrichment was gained after triboelectrostatic separation on both subbituminous coals, but the effect was more obvious in Zhundong coal than in Shenfu coal. The inertinite content of tailings in Zhundong coal reached over 60%, and the total sodium content of tailings was 3551 $\mu\text{g/g}$, one third higher than that of clean coal, due to the close relationship between sodium and inertinite. It was demonstrated that sodium in Zhundong coal, especially the $\text{H}_2\text{O-Na}$ that causes ash-forming issues in combustion, could be removed after maceral separation, and the products could be used as vitrinite-rich and inertinite-rich materials for coal-staged utilization.

Author Contributions: Conceptualization, X.H.; Methodology, X.H.; Validation, W.W. and P.D.; Formal Analysis, X.H.; Investigation, X.H. and Y.Y.; Resources, J.H.; Data Curation, C.Z.; Writing—Original Draft Preparation, X.H.; Writing—Review and Editing, W.W., C.Z. and Q.L.; Visualization, Y.Y. and P.D.; Supervision, W.W.; Project Administration, W.W.; Funding Acquisition, X.H. and Y.Y. All authors have read and agreed to the published version of the manuscript.

Funding: This research is supported by National Natural Science Foundation of China (No. U1903207, No. 42002184, No. 41972176, No. 92062109, and No. 52074289), Natural Science Foundation of Jiangsu Province (No. BK20200638), Fundamental Research Funds for the Central Universities (No. 2020CXNL11), and A Project Funded by the Priority Academic Program Development of Jiangsu Higher Education Institutions.

Acknowledgments: We are very grateful to all the editors and reviewers who have helped us improve and publish this paper.

Conflicts of Interest: The authors declare no conflict of interest.

References

- Li, J.B.; Zhu, M.M.; Zhang, Z.Z.; Zhang, K.; Shen, G.Q.; Zhang, D.K. The mineralogy, morphology and sintering characteristics of ash deposits on a probe at different temperatures during combustion of blends of zhundong lignite and a bituminous coal in a drop tube furnace. *Fuel Process. Technol.* **2016**, *149*, 176–186. [[CrossRef](#)]
- Yang, Y.M.; Wu, Y.X.; Zhang, H.; Zhang, M.; Liu, Q.; Yang, H.R.; Lu, J.F. Improved sequential extraction method for determination of alkali and alkaline earth metals in zhundong coals. *Fuel* **2016**, *181*, 951–957. [[CrossRef](#)]
- Li, J.; Zhuang, X.G.; Querol, X.; Font, O.; Moreno, N.; Zhou, J.B.; Lei, G.M. High quality of Jurassic coals in the southern and eastern Junggar coalfields, Xinjiang, NW China: Geochemical and mineralogical characteristics. *Int. J. Coal Geol.* **2012**, *99*, 1–15. [[CrossRef](#)]
- Ge, H.J.; Shen, L.H.; Gu, H.M.; Song, T.; Jiang, S.X. Combustion performance and sodium absorption of ZhunDong coal in a CLC process with hematite oxygen carrier. *Appl. Therm. Eng.* **2016**, *94*, 40–49. [[CrossRef](#)]
- Zhu, C.; Qu, S.J.; Zhang, J.; Wang, Y.; Zhang, Y.H. Distribution, occurrence and leaching dynamic behavior of sodium in zhundong coal. *Fuel* **2017**, *190*, 189–197. [[CrossRef](#)]
- Fan, Y.Q.; Zhang, H.X.; Lyu, Q.G.; Zhu, Z.P. Investigation of slagging characteristics and anti-slagging applications for Indonesian coal gasification. *Fuel* **2020**, *267*, 117285. [[CrossRef](#)]
- Liu, D.B.; Li, W.; Li, S.Y.; Song, W.H.; Liu, D.F.; Kong, R.J. Transformation characteristics of sodium, chlorine and sulfur of zhundong coal during O₂/CO₂ combustion in circulating fluidized bed. *Energy* **2019**, *185*, 254–261. [[CrossRef](#)]
- Dai, S.F.; Liu, J.; Ward, C.R.; Hower, J.C.; Xie, P.; Jiang, Y.; Hood, M.M.; O’Keefe, J.M.K.; Song, H. Petrological, geochemical, and mineralogical compositions of the low-Ge coals from the Shengli Coalfield, China: A comparative study with Ge-rich coals and a formation model for coal-hosted Ge ore deposit. *Ore Geol. Rev.* **2015**, *71*, 318–349. [[CrossRef](#)]
- Liu, Z.; Li, J.B.; Wang, Q.H.; Lu, X.F.; Zhang, Y.Y.; Zhu, M.M.; Zhang, Z.Z.; Zhang, D.K. An experimental investigation into mineral transformation, particle agglomeration and ash deposition during combustion of Zhundong lignite in a laboratory-scale circulating fluidized bed. *Fuel* **2019**, *243*, 458–468. [[CrossRef](#)]
- Song, G.L.; Yang, S.B.; Song, W.J.; Qi, X.B. Release and transformation behaviors of sodium during combustion of high alkali residual carbon. *Appl. Therm. Eng.* **2017**, *122*, 285–296. [[CrossRef](#)]
- Qi, X.B.; Song, G.L.; Yang, S.B.; Yang, Z.; Lyu, Q.G. Migration and transformation of sodium and chlorine in high-sodium high-chlorine xinjiang lignite during circulating fluidized bed combustion. *J. Energy Inst.* **2018**, *92*, 673–681. [[CrossRef](#)]
- Song, G.L.; Qi, X.B.; Song, W.J.; Yang, S.B. Slagging and fouling of Zhundong coal at different air equivalence ratios in circulating fluidized bed. *Fuel* **2017**, *205*, 46–59. [[CrossRef](#)]
- Tang, C.W.; Pan, W.G.; Zhang, J.K.; Wang, W.H.; Sun, X.L. A comprehensive review on efficient utilization methods of High-alkali coals combustion in boilers. *Fuel* **2022**, *316*, 123269. [[CrossRef](#)]
- Li, G.D.; Li, S.Q.; Huang, Q.; Yao, Q. Fine particulate formation and ash deposition during pulverized coal combustion of high-sodium lignite in a down-fired furnace. *Fuel* **2015**, *143*, 430–437. [[CrossRef](#)]
- Ma, D.Y.; Ruan, R.H.; Li, Y.D.; Zhang, L.; Wang, X.B.; Zi, J.B.; Wang, Y.B.; Li, H.; Wen, H.B.; Tan, H.Z. Characteristics of fine particle formation during combustion of xinjiang high-chlorine-sodium coal. *Fuel* **2021**, *297*, 120772. [[CrossRef](#)]
- Gao, Q.; Li, S.Q.; Yuan, Y.; Zhang, Y.Y.; Yao, Q. Ultrafine particulate matter formation in the early stage of pulverized coal combustion of high-sodium lignite. *Fuel* **2015**, *158*, 224–231. [[CrossRef](#)]
- Li, X.; Bai, Z.Q.; Bai, J.; Han, Y.N.; Kong, L.X.; Li, W. Transformations and roles of sodium species with different occurrence modes in direct liquefaction of Zhundong coal from Xinjiang, Northwestern China. *Energy Fuels* **2015**, *29*, 5633–5639. [[CrossRef](#)]
- Liang, D.C.; Xie, Q.; Zhou, H.B.; Yang, M.S.; Cao, J.Y.; Zhang, J. Catalytic effect of alkali and alkaline earth metals in different occurrence modes in Zhundong coals. *Asia-Pac. J. Chem. Eng.* **2018**, *13*, e2190. [[CrossRef](#)]
- Feng, Z.H.; Pang, K.L.; Bai, Z.Q.; Hou, R.R.; Ye, D.H.; Guo, Z.X.; Kong, L.X.; Bai, J.; Li, W. Occurrence and transformation of sodium and calcium species in mild liquefaction solid product of hami coal during pyrolysis. *Fuel* **2021**, *286*, 119489. [[CrossRef](#)]
- Lin, X.C.; Luo, M.; Li, S.Y.; Yang, Y.P.; Chen, X.J.; Tian, B.; Wang, Y.G. The evolutionary route of coal matrix during integrated cascade pyrolysis of a typical low-rank coal. *Appl. Energy* **2017**, *199*, 335–346. [[CrossRef](#)]
- Li, S.; Chen, S.J.; Jin, J.; Li, T.Y.; Chen, Y.Y.; Ma, S.L. The Jurassic oil-source correlation of Dishuiquan Oilfield in Junggar basin, Northwest China. *Pet. Sci. Technol.* **2020**, *38*, 354–360. [[CrossRef](#)]
- Guo, H.N.; Shi, H.; Wu, Y.X.; Lyu, J.F.; Zhang, Y. Mineral transformation during rapid heating and cooling of Zhundong coal ash. *Fuel* **2022**, *310*, 122269. [[CrossRef](#)]
- Zhang, Z.K.; Tang, M.T.; Yang, Z.Y.; Ma, J.; Liu, L.N.; Shen, B.X. SO₂ and NO emissions during combustion of high-alkali coal over a wide temperature range: Effect of Na species and contents. *Fuel* **2022**, *309*, 122212. [[CrossRef](#)]
- Zhou, J.B.; Zhuang, X.G.; Alastuey, A.; Querol, X.; Li, J.H. Geochemistry and mineralogy of coal in the recently explored Zhundong large coal field in the Junggar basin, Xinjiang province, China. *Int. J. Coal Geol.* **2012**, *82*, 51–67. [[CrossRef](#)]
- Zhang, D.; Zhou, J.; Yi, X.; Zhao, L.; Song, Z.; Li, B. The braided river delta-shallow lake depositional system of middle Jurassic Xishanyao formation in the Xiheishan coal district, eastern Junggar coal field, Xinjiang. *Inn. Mong. Petrochem.* **2009**, *9*, 105–108.
- Peng, W.L.; Guo, F.T.; Hu, G.Y.; Lyu, Y.; Gong, D.Y.; Liu, J.Y.; Feng, Z.Q.; Guo, J.G.; Guo, Y.C.; Hang, W.X. Geochemistry and accumulation process of natural gas in the shenmu gas field, ordos basin, central China. *J. Pet. Sci. Eng.* **2019**, *180*, 1022–1033. [[CrossRef](#)]

27. Dai, S.F.; Ren, D.Y.; Chou, C.L.; Li, S.S.; Jiang, Y.F. Mineralogy and geochemistry of the No. 6 coal (Pennsylvanian) in the Jungar Coalfield, Ordos Basin, China. *Int. J. Coal Geol.* **2006**, *66*, 253–270. [[CrossRef](#)]
28. Akhtar, S.; Yang, X.Y.; Pirajno, F. Sandstone type uranium deposits in the Ordos Basin, Northwest China: A case study and an overview. *J. Asian Earth Sci.* **2017**, *146*, 367–382. [[CrossRef](#)]
29. Wang, X.M.; Jiao, Y.Q.; Wu, L.Q.; Rong, H.; Wang, X.M.; Song, J. Rare earth element geochemistry and fractionation in jurassic coal from dongsheng–shenmu area, ordos basin. *Fuel* **2014**, *136*, 233–239. [[CrossRef](#)]
30. Wang, X.M.; Wang, X.M.; Pan, S.D.; Yang, Q.; Hou, S.H.; Jiao, Y.Q.; Zhang, W.M. Occurrence of analcime in the middle jurassic coal from the dongsheng coalfield, northeastern ordos basin, China. *Int. J. Coal Geol.* **2018**, *196*, 126–138. [[CrossRef](#)]
31. Yang, R.C.; Han, Z.Z.; Li, Z.X.; Fan, A.P. Base-level cycles and episodic coal accumulation—Case study of Dongsheng Coalfield in Ordos Basin. *J. China Univ. Min. Technol.* **2006**, *16*, 439–442. [[CrossRef](#)]
32. He, X.; Sun, H.; Chen, X.W.; Zhao, B.; Zhang, X.X.; Komarneni, S. Charging mechanism analysis of macerals during triboelectrostatic enrichment process: Insights from relative dielectric constant, specific resistivity and X-ray diffraction. *Fuel* **2018**, *225*, 533–541. [[CrossRef](#)]
33. He, X.; Sun, H.; Zhao, B.; Chen, X.W.; Zhang, X.X.; Komarneni, S. Tribocharging of macerals with various materials: Role of surface oxygen-containing groups and potential difference of macerals. *Fuel* **2018**, *233*, 750–768. [[CrossRef](#)]
34. Chen, X.W.; Zhuang, X.G.; Zhou, J.B.; Zeng, X.J.; Amina; Ge, D.F.; Li, X.; Yang, S. Coal quality and its distribution of the eastern Junggar coalfield in Junggar basin, Xinjiang. *Xinjiang Geol.* **2013**, *31*, 89–93.
35. He, X.; Zhang, X.X.; Jiao, Y.; Zhu, J.S.; Chen, X.W.; Li, C.Y.; Li, H.S. Complementary analyses of infrared transmission and diffuse reflection spectra of macerals in low-rank coal and application in triboelectrostatic enrichment of active maceral. *Fuel* **2017**, *192*, 93–101. [[CrossRef](#)]
36. ICCP. The new vitrinite classification (ICCP System 1994). *Fuel* **1998**, *77*, 349–358. [[CrossRef](#)]
37. ICCP. The new inertinite classification (ICCP System 1994). *Fuel* **2001**, *80*, 459–471. [[CrossRef](#)]
38. Pickel, W.; Kus, J.; Flores, D. Classification of liptinite-ICCP System 1994. *Int. J. Coal Geol.* **2017**, *169*, 40–61. [[CrossRef](#)]
39. Sykorova, I.; Pickel, W.; Christianis, K.; Wolf, M.; Taylor, G.H.; Flores, D. Classification of huminite-ICCP System 1994. *Int. J. Coal Geol.* **2005**, *62*, 85–106. [[CrossRef](#)]
40. Benson, S.A.; Holm, P.L. Comparison of inorganics in three low-rank coals. *Ind. Eng. Chem. Prod. Res. Dev.* **1985**, *24*, 145–149. [[CrossRef](#)]
41. Zhang, J.; Han, C.L.; Yan, Z.; Liu, K.L.; Xu, Y.Q.; Sheng, C.D.; Pan, W.P. The varying characterization of alkali metals (Na, K) from coal during the initial stage of coal combustion. *Energy Fuels* **2001**, *15*, 786–793. [[CrossRef](#)]
42. Dai, S.F.; Li, D.H.; Ren, D.Y.; Tang, Y.G.; Shao, L.Y.; Song, H.B. Geochemistry of the late Permian No. 30 coal seam, Zhijin Coalfield of Southwest China: Influence of a siliceous low temperature hydrothermal fluid. *Appl. Geochem.* **2004**, *19*, 1315–1330. [[CrossRef](#)]
43. Li, Z.; Ward, C.R.; Gurba, L.W. Occurrence of non-mineral inorganic elements in macerals of low-rank coals. *Int. J. Coal Geol.* **2010**, *81*, 242–250. [[CrossRef](#)]
44. Grigore, M.; Sakurovs, R. Inorganic matter in victorian brown coals. *Int. J. Coal Geol.* **2016**, *154–155*, 257–264. [[CrossRef](#)]
45. Ward, C.R. Analysis and significance of mineral matter in coal seams. *Int. J. Coal Geol.* **2002**, *50*, 135–168. [[CrossRef](#)]
46. Finkelman, R.B.; Palmer, C.A.; Wang, P. Quantification of the modes of occurrence of 42 elements in coal. *Int. J. Coal Geol.* **2018**, *185*, 138–160. [[CrossRef](#)]
47. Matsuoaka, K.; Rosyadi, E.; Tomita, A. Mode of occurrence of calcium in various coals. *Fuel* **2002**, *81*, 1433–1438. [[CrossRef](#)]
48. Wijaya, N.; Choo, T.K.; Zhang, L. Generation of ultra-clean coal from Victorian brown coal—sequential and single leaching at room temperature to elucidate the elution of individual inorganic elements. *Fuel Process. Technol.* **2011**, *92*, 2127–2137. [[CrossRef](#)]
49. Wijaya, N.; Choo, T.K.; Zhang, L. Generation of ultra-clean coal from Victorian brown coal: Effect of hydrothermal treatment and particle size on coal demineralization and the extraction kinetic of individual metals. *Energy Fuel* **2012**, *26*, 5028–5035. [[CrossRef](#)]
50. Dai, S.F.; Ren, D.Y.; Chou, C.L.; Finkelman, R.B.; Seredin, V.V.; Zhou, Y.P. Geochemistry of trace elements in chinese coals: A review of abundances, genetic types, impacts on human health, and industrial utilization. *Int. J. Coal Geol.* **2012**, *94*, 3–21. [[CrossRef](#)]
51. Chou, C.L. Sulfur in coals: A review of geochemistry and origins. *Int. J. Coal Geol.* **2012**, *100*, 1–13. [[CrossRef](#)]
52. Yuan, W.; Li, J.; Zhuang, X.G.; Yang, G.H.; Pan, L. Geological controls on mineralogical characteristic differences of coals from the main coal fields in shaanxi, north China. *Energies* **2021**, *14*, 7905. [[CrossRef](#)]
53. Wang, W.F.; Sang, S.X.; Bian, Z.F.; Duan, P.P.; Qian, F.C.; Lei, S.G.; Qin, Y. Fine-grained pyrite in some Chinese coals. *Energy Explor. Exploit.* **2016**, *34*, 543–560. [[CrossRef](#)]

Disclaimer/Publisher’s Note: The statements, opinions and data contained in all publications are solely those of the individual author(s) and contributor(s) and not of MDPI and/or the editor(s). MDPI and/or the editor(s) disclaim responsibility for any injury to people or property resulting from any ideas, methods, instructions or products referred to in the content.